Accepted Article

Authors: Rosa Arrigo, Simone Gallarati, Manfred E Schuster, Jake Seymour, Diego Gianolio, Ivan da Silva, June Callison, Haosheng Feng, John E Proctor, Pilar Ferrer, Federica Venturini, dave grinter, and Georg Held

A Journal of

ChemPubSoc
Europe

WILEY-VCH   www.chemcatchem.org

Influence of synthesis conditions on the structure of nickel nanoparticles and their reactivity in selective asymmetric hydrogenation

Rosa Arrigo,*[a,b] Simone Gallarati,[c] Manfred E. Schuster,[b,d] Jake Seymour,[e] Diego Gianolio,[b] Ivan da Silva,[f] June Callison,[g,h] Haosheng Feng,[i] John E. Proctor,[a] Pilar Ferrer,[b] Federica Venturini,[b] David Grinter[b] and Georg Held[d,b]

Abstract: Unsupported and SiO$_2$-supported Ni nanoparticles (NPs), were synthesised *via* hot-injection colloidal route using oleylamine (OAm) and trioctylphosphine (TOP) as reducing and protective agents, respectively. By adopting a multi-length scale structural characterization, it was found that by changing equivalents of OAM and TOP not only the size of the nanoparticles is affected but also the Ni electronic structure. The synthetized NPs were modified with (*R,R*)-tartaric acid (TA) and investigated in the asymmetric hydrogenation of methyl acetoacetate to chiral methyl-3-hydroxy butyrate. The comparative analysis of structure and catalytic performance for the synthetized catalysts has enabled us to identify a Ni metallic active surface, whereby the activity increases with the size of the metallic domains. Conversely, at the high conversion obtained for the unsupported NPs no impact of particle size on the selectivity was observed. (*R*)-selectivity was very high only on catalysts containing positively charged Ni species such as over the SiO$_2$-supported Ni oxide NPs. This work shows that the chiral modification of metallic Ni NPs with TA is insufficient to maintain high selectivity towards the (*R*)-enantiomer at long reaction time and provide guidance for the engineering of long-term stable enantioselective catalysts.

Introduction

The enantioselective asymmetric hydrogenation of unsaturated molecules is broadly applied for the synthesis of pharmaceuticals and fine chemicals, where the biggest challenge is attaining total selectivity to one specific enantiomer.[1] One of the most studied examples of such reactions is the hydrogenation of β-ketoesters over nickel-based catalysts,[2] e.g. methyl acetoacetate (MAA) to methyl-3-hydroxybutyrate (MHB), shown in scheme 1. MHB is an important intermediate in the synthesis of carbonic anhydrase inhibitor MK-0507, used in the treatment of glaucoma;[3] moreover, 3-hydroxyacids are useful building blocks in chiral synthesis.[4]
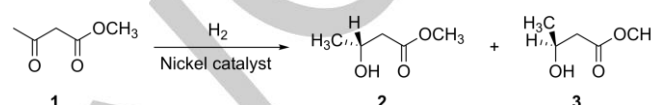
Scheme 1. Hydrogenation of pro-chiral β-ketoester methyl acetoacetate gives two enantiomers, (*R*)- and (*S*)-methyl-3-hydroxybutyrate. When the surface of the nickel catalyst is modified with (*R,R*)-tartaric acid (also in combination with an inorganic salt such as NaBr), the (*R*)-enantiomer is preferably obtained.

This reaction can be carried out with high enantiomeric excess (*ee*) if the surface of the nickel catalyst, e.g. Raney Ni or supported nanoparticles (NPs), is modified with a chiral molecule, typically (*R,R*)-tartaric acid or an amino acid, or by selective poisoning using inorganic salts, such as sodium bromide.[5] A molecular level understanding of this reaction would be beneficial to tackle the challenge of achieving total selectivity. Particularly, the mechanism by which enantioselectivity is realized at the Ni catalyst surface aided by modifiers is still subject to much debate.[6-9] Investigations of adsorbates structures of tartaric acid and MAA on model single crystal Ni surfaces have highlighted two possible pathways through which the chiral molecule of the modifier facilitates the formation of the (*R*)-enantiomer: a) through a one-to-one molecular interaction, the chiral tartrate molecules adsorbed on the Ni surface controls the adsorption geometry of the pro-chiral reagent, which is then reduced on the adjacent exposed metallic Ni surface by chemisorbed H atoms; b) the chiral molecules forming a supramolecular chiral arrangement on the Ni surface desorb from the largely ordered Ni terraces leaving a chiral Ni surface structure responsible for the specific chemisorption of the reagent with the favorable geometry;[7] c) the interaction of tartrate with oxidised Ni particles facilitates etching of Ni cations from the surface leaving naturally chiral kinks sites on the Ni surface responsible for enantioselectivity.[9]

Moreover, Keane et al. [9] found that molecular Ni species leached out during modification manifest enantio-selective activity. This suggests that cationic Ni species might also be involved in the catalytic reaction.

Despite the large volume of literature available on the adsorption and ordering of chiral molecules on single crystals a direct structure-activity correlation remains undisclosed. On the one hand, the complexity of a real catalytic system makes it difficult to unveil the local arrangement of these on their surface. On the other hand, catalytic performances are only available for real catalysts such as supported Ni catalysts. [10] In contrast to single crystals, structurally ill-defined nanoparticles (NPs) enable measurable conversions but suffer from poor enantiomeric

[a]   Dr R. Arrigo, and Dr J. E. Proctor, School of Sciences, Engineering and Environment, University of Salford, Manchester M5 4WT, UK
       Correspondence to E-mail: r.arrigo@salford.ac.uk
[b]   Dr R. Arrigo, Dr M. E. Schuster, Dr D. Gianolio, Dr P. Ferrer Escourieula, Dr F. Venturini, Dr D. Grinter, Prof. G. Held, Diamond Light Source, Harwell Science and Innovation Campus, Didcot OX11 0DE, UK
[c]   S. Gallarati, School of Chemistry, University of St Andrews, North Haugh, St Andrews KY16 9ST, UK
[d]   Dr M. E. Schuster, Johnson Matthey Technology Centre, Reading RG4 9NH, UK
[e]   J. Seymour, Department of Chemistry, University of Reading, Reading RG6 6AD, UK
[f]   Dr I. da Silva, ISIS Facility, Rutherford Appleton Laboratory, Chilton, Didcot OX11 0QX, UK
[g,h] Dr J. Callison, Department of Chemistry, University College London, 20 Gordon Street, London, WC1H 0AJ, UK, and UK Catalysis Hub, Research Complex at Harwell (RCaH), Rutherford Appleton Laboratory, Harwell Oxon, OX11 0FA, UK
[i]   H. Feng, Department of Chemistry, University of Cambridge, Cambridge, CB2 1EW, UK

       Supporting information for this article is given *via* a link at the end of the document.

selectivity if compared to Raney Ni.[11] The surface modification proved also in the case of the NPs to influence selectivity and conversion.[12] Yet, it is unclear whether macroscopically achiral symmetrically round-like NPs with high-index surface sites might create more opportunities for the generation of enantioselective surface ensembles upon chiral modification. Moreover, round-like NPs of different sizes enable a different population of kinks sites as well as a different size of the facets, both leading to a different mechanism of action of the TA modifier. An understanding of the impact of NPs size, electronic and crystallographic structure and morphology on the catalytic performance of chirally modified NPs is missing, whilst it can provide important insights for the design of improved enantioselective catalysts. Our aim is to contribute a systematic study of NPs structure-activity correlations, which will enable new mechanistic insights into the catalyst's selective chiral function and the structural transformations responsible for performance degradation. In this work, we synthetize supported and unsupported nickel nanoparticles of different size and investigate their catalytic performance and physicochemical properties, such as morphology, size and structure, using synchrotron-based X-ray absorption near edge structure (XANES), extended X-ray absorption fine structure (EXAFS) spectroscopies and X-ray photoelectron spectroscopy (XPS), in combination with bright field scanning transmission electron microscopy (BF-STEM), high angle annular dark field scanning transmission electron microscopy (HAADF-STEM) and X-ray diffraction (XRD).

For a precise control over materials properties at the nanometer level (NPs with narrow size distribution, morphology and composition), we employed the hot-injection colloidal synthesis,[13] which is based on the reduction of metallorganic or metal salt precursors in high-boiling nonpolar solvents in the presence of surfactant agents.[14] Rapid injection results in a supersaturated solution where the nucleation of the particles occurs within a short time period. The surfactant molecules capped around the nanocrystals prevent their agglomeration and protect them from possible oxidation upon exposure to atmospheric conditions. Moreover, the surfactant molecules endow the NPs with good colloidal stability.[15]

We will show that by modifying the synthetic composition, it is possible to tune the NPs' size, as well as the Ni electronic structure. These have significant implications on the resulting reactivity in the investigated reaction.

Results and Discussion

A series of unsupported and SiO₂-supported Ni NPs were synthesized using the hot-injection method to control the size of the NPs by changing the ratio between the reducing (oleylamine, OAm) and protecting agents (trioctylphosphine, TOP).

Table 1 lists the synthetic conditions and samples' notation. The detailed synthetic procedure is reported in the experimental section. Firstly, we will discuss the impact of the composition of the synthesis mixture on the structural features of the resulting unsupported and SiO₂-supported Ni NPs. These will then be correlated with the catalytic performance reported subsequently. To the best of our knowledge, this is the first time that the hot-injection oleylamine-trioctylphosphine Ni NPs synthesis has

been used to prepare nanoparticles to be modified with tartaric acid and to catalyze the hydrogenation of methyl acetoacetate.

Table 1. Synthetic conditions and resulting size of Ni NPs.			
Samples	**OAm[b] (x) [eq.]**	**TOP[c] (y) [eq.]**	**Size[d/e] [nm]**
Ni_2.5x1.5y	2.5	1.5	1.3/8.0±1.4
Ni_5x1.5y	5	1.5	4.0/7.0±1.3
Ni_10x1.5y	10	1.5	5.6/10.6±1.9
Ni/SiO₂_5x1.5y[a]	5	1.5	4.7/9.9±1.8
Ni/SiO₂_5x0.75y[a]	5	0.75	7.3[f]; 2.5[g]/2.2±0.6
Ni/SiO₂_5x3y[a]	5	3	3.8/6.5±0.7
[a] 10 wt% loading on CAB-O-SIL 5M silica. [b] Total number of equivalents of oleylamine (OAm) and 1-octadecene (21) kept constant by varying amount of solvent. [c] Trioctylphosphine. [d] Determined by XRD. [e] Determined by HAADF-STEM. Average particle size of Ni metal [f] and Ni oxide [g], respectively.			

Traditionally, this synthetic method is performed on a small scale (mmol of nickel precursors, mg of NPs produced) and the NPs are isolated unsupported *via* flocculation procedure, which removes the high-boiling solvent and excess ligands.[16] We employ the mid-to-high temperature thermal decomposition of Ni(acac)₂ with OAm-TOP as it has been reported to be one of the best strategies for controlling the production of highly monodisperse NPs with narrow size distribution, morphology and composition.[17] However, as it is preferable to produce larger amounts of catalyst for testing, multiple spectroscopic and structural characterizations, we attempted to scale up this well-known synthesis (gram scale) and also support the colloidal NPs on silica for ease of handling.

Structural characterization of unsupported NPs

The low magnification (LM) scanning transmission electron microscopy characterization of the unsupported Ni_5x1.5y catalyst is reported in Figures S1a and b of the supporting information. Accordingly, the NPs appear spherical in shape, or slightly elongated, and have a core-shell structure, where the core is composed of Ni encapsulated in a less than 1 nm thick and rough shell of lower contrast, presumably originating from the capping agents as indicated by XPS and NEXAFS analysis at the C1s and O1s core levels (not shown).

A closer inspection using high resolution high angle annular dark field scanning transmission electron microscopy (HAADF-STEM) (Figure 1a and 1b) enables us to identify detailed structural features for this catalyst. Particularly, Figures 1a shows that the oval NPs is in fact a twinned cuboctahedron with several parallel twin lamellae (as indicated by the arrow) accounting for the anisotropic elongation of the NPs along the C2 axis of the twin. Figures 1b shows in detail the shell structure, where Ni nanocrystallites are embedded within the organic shell, giving it the roughened aspect seen in the LM STEM images. The Ni_10x1.5y sample shows the biggest NPs with more abundantly elongated particles (LM HR STEM in Figures S1c and S1d). The HR-HAADF STEM images in Figures 1c shows a round NPs marked by the arrow imaged along common 5-fold axis of a multiply twinned decahedron, composed of 5 face-

2

sharing tetrahedrons. Figure 1d shows an example of twinned NPs composed of face-sharing tetrahedrons and cuboctahedron. Note that in this case, the faces of the octahedron and the tetrahedrons do not match perfectly at the grain boundaries, but an interfacial layer of lower contrast is observed, which is probably due to the residual capping agent (Figure 2f).
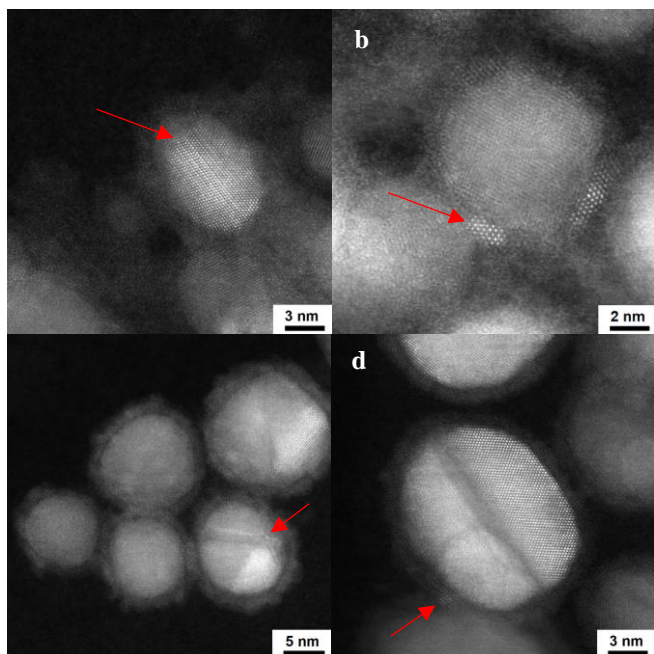

Figure 1. a) and b): HR-HAADF-STEM characterization of Ni_5x1.5y. The arrow indicates the twinned lamellae of the NPs in a) and a smaller Ni NPs embedded in the organic shell in b; c) and d): HR-HAADF-STEM characterization of Ni_10x1.5y. In a) the arrow indicates the 5-fold axis of a multiply twinned decahedron. In b) the arrow indicates the Ni atoms of a smaller NPs embedded in the organic shell.

A roughened shell of abundant nano-clusters embedded in the organic shell (Figures 1c and 1d) is also seen in this sample.

In comparison, the LM STEM images of the Ni_2.5x1.5y sample (Figure 2) show mainly round amorphous core-shell NPs where the presence of additional nano-clusters embedded in the organic shell is rarely encountered. Peculiarly in this sample, some of the NPs show an inner region of lower contrast, indicating the presence of voids (Figure 2a and b) within the Ni NPs or an area of localized low-density elements such as encapsulated organic matter.

XRD (Figure 3a) confirms the successful formation of metallic Ni nanoparticles without the need of further reduction steps during the synthesis. Particularly, in samples Ni_5x1.5y and Ni_10x1.5y, the peaks at 44.4 and 51.7 degrees 2θ are the characteristic (111) and (200) reflections of metallic nickel, respectively.[18] In Ni_2.5x1.5y, only the most intense (111) reflection is distinguishable, due to peak broadening caused by the smaller crystallite size. Furthermore, no significant contribution from ordered Ni oxide was observed in the XRD patterns of the unsupported NPs.

The average crystallite size determined by STEM for the three samples follows the order of Ni_5x1.5y ≤ Ni_2.5x1.5y < Ni_10x1.5y, as summarized in Table 1. This is in sharp contrast with the size of the coherent crystalline domains determined by

XRD. The different trends in average particle size determined by STEM and XRD led us to conclude that significant fractions of the particles are an amorphous phase and that this is the predominant phase in the Ni_2.5x1.5y sample.
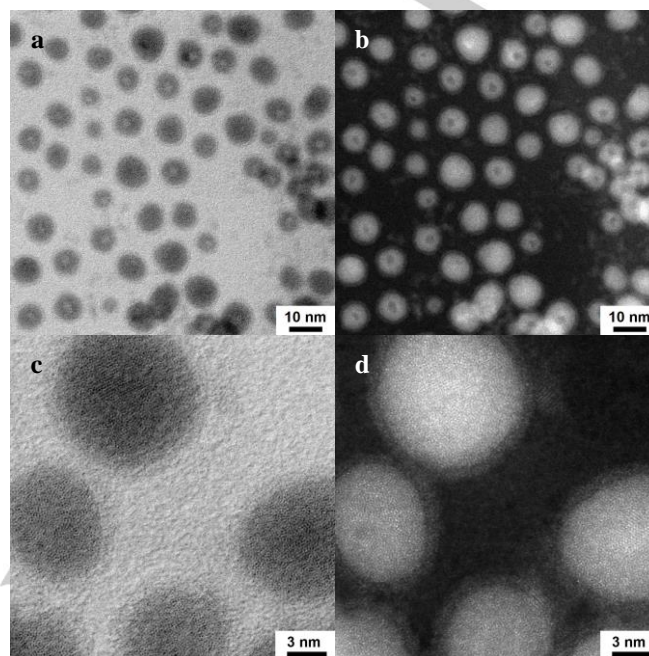

Figure 2. STEM characterization of Ni_2.5x1.5y. LM BF-STEM a) and corresponding HAADF-STEM b); HR BF-STEM of a Ni NPs in c) and corresponding HAADF-STEM d).

The trend in particle size observed for Ni_5x1.5y and Ni_10x1.5y is consistent with our expectation upon the systematic variation of the x:y ratio (with x and y being the number of equivalents of OAm and TOP, respectively), as investigated in these experiments. In the colloidal synthesis of nanoparticles, the growth mechanism is generally divided into several stages, occurring at different time frames: nucleation, aggregation growth, and possibly also Ostwald ripening process.[19] While OAm is expected to control the nucleation rate and growth, TOP acts as capping agent and provides tunable surface stabilization through coordination with the Ni surface, thus hindering the growth. A small OAm:TOP (x:y) ratio during the synthesis leads to small NPs, as in the Ni_5x1.5y catalyst, since the relatively more abundant capping agent TOP further hinders aggregation and growth. Conversely, increasing the x:y ratio leads to larger particles, as in Ni_10x1.5y, since the amount of capping agent is relatively decreased, along with its ability to kinetically control the growth step by steric hindrance. Furthermore, by increasing the amount of OAm, the nucleation rate is enhanced, thus larger quantities of nuclei are produced in solution; such small nuclei are unstable due to the high surface energy and intermolecular forces, leading to growth or rapid aggregation of the nickel nanoparticles[20] and even formation of twinned structures, as observed in this study. The amount of reducing agent also influences the geometry of the primary nucleus: whilst at a low concentration, the nuclei grow to form small tetrahedrons, which aggregate forming multiply-twinned NPs, with larger amounts of reducing agent the bigger and more thermodynamically favored cub-octahedrons are formed as well

3

as largely elongated twinned particles (Figures S1c and S1d). Interestingly, when the amount of reducing agent is as low as 2.5 equivalents with respect to the Ni(acac)$_2$ precursor, as in Ni_2.5x1.5y, the NPs' formation mechanism is different from the one described above. To understand the formation of amorphous NPs in this condition, one should bear in mind that TOP not only acts as a capping agent to prevent NPs' growth, but also as a source of phosphorous in the synthesis of metal phosphides.[21] In the case of Ni phosphides, following the initial formation of the Ni metallic core upon Ni precursor decomposition, a subsequent phosphidation step occurs, during which, the voids observed are formed through the Kirkendall effect, where outward diffusion of metal atoms from the core is faster than inward diffusion of reactive species.[22]

HAADF-STEM energy dispersive X-ray (EDX) mapping in Figure 3b confirms the colocation of P and Ni atoms, whereas little signal from O or C is observed, confirming the presence of a predominant Ni phosphide phase, which is amorphous as shown in Figure 2c and 2d.
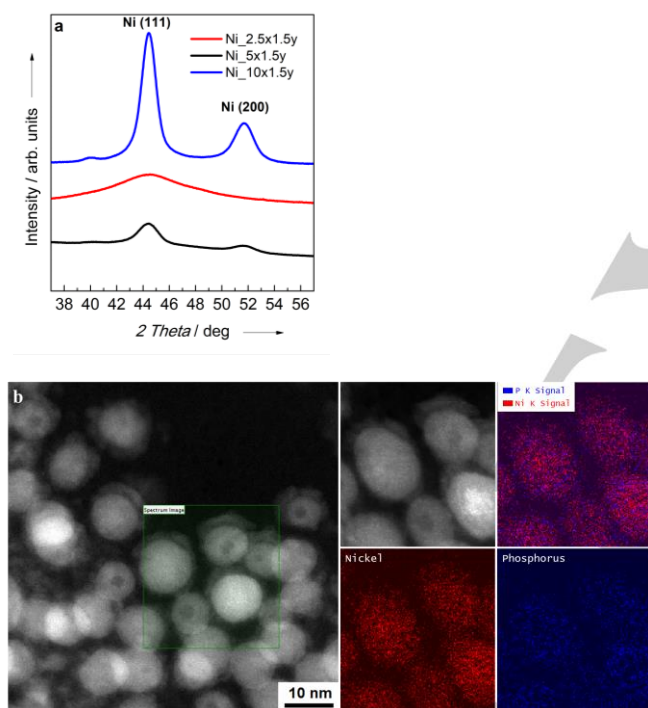

Figure 3. a) XRD characterization; b) HAADF-STEM and EDX elemental mapping for the sample Ni_2.5x1.5y.

Raman spectra of the Ni_2.5x1.5y sample (Figure S2) exhibited a peak corresponding to the most intense mode in amorphous NiPS3 at ca. 600 cm^{-1},[23] confirming the existence of Ni-P bonds in this sample. We did not observe the weaker peak at ca. 380 cm^{-1} seen in amorphous NiPS3, suggesting that the Ni phosphide in this sample is more amorphous in character than that in the previous work.[21] We collected 5 spectra from different locations of the sample and all spectra exhibited similar features. Raman spectra of the other samples revealed no evidence for the presence of a Ni phosphide phase.
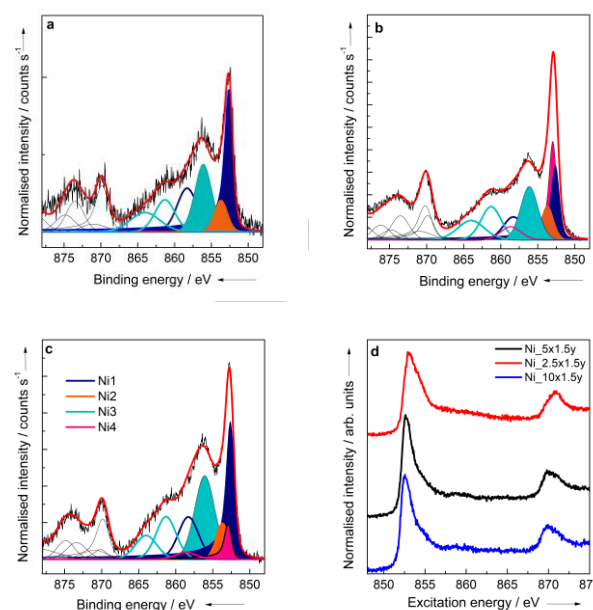

Figure 4. Fitted Ni 2p XP spectra (KE 570 eV) for Ni_10x1.5y (a); Ni_2.5x1.5y (b) and Ni_5x1.5y (c). Fitting: N1 (852.6 eV) is Ni^0; N2 (852.9 eV) is Ni-P; N3 (853.7 3V) is Ni^{2+} and Ni4 (856.1 eV) is Ni^{2+}/Ni^{3+} in oxide and oxyhydroxide, respectively. Ni L edges NEXAFS spectra for all samples in (d).

The spin-orbit split Ni2p XPS and NEXAFS characterizations of the as synthetized samples in Figure 4 confirm these findings, whilst providing additional information about the nature of the Ni phosphide phase. We first describe the surface sensitive Ni2p XPS spectrum of the Ni_10x1.5y sample (Figure 4a). The main metallic Ni 2p$_{3/2}$ peak (Ni1) is found at the binding energy of 852.6 eV, consistently with the literature.[24] An additional satellite peak attributed to 3d → 4s excitation[24] was found at 5.6 eV above the main line in a reference Ni polycrystalline foil (not shown) and included here in the fitting of the NPs spectra.

A relatively less abundant component Ni2 was found at 853.7 eV, whilst a more abundant component Ni3 was found at 856.1 eV, which is accompanied by two intense satellite peaks at 861.1 eV and 864 eV. Based on literature assignments,[24-25] the Ni2 component at 853.7 eV is due to Ni$^{(II)}$ in NiO, whereas the Ni3 component at 856.1 eV is due to a mixed Ni$^{(II)}$/Ni$^{(III)}$ oxy-hydroxide phase. A closer inspection of the spectrum of the Ni_2.5x1.5y sample, which is compared to that of Ni_5x1.5y in Figure S3, reveals the presence of an additional Ni$^{\delta+}$ component (Ni4) at 852.95 eV and corresponding low intensity satellite component at 860.5 eV, previously attributed to Ni phosphides [26]. Note that the same 4 component fitting was applied to all three samples; while only a small contribution of the Ni4 component was needed to afford a good fit of the Ni_5x1.5y spectrum (Figure 4c), the fit of the Ni_10x1.5y spectrum (Figure 4a) suggests that this component is apparently absent in this case, within the volume probed by these XPS measurements. Since the kinetic energy of the photoelectrons in the present XPS analysis (hυ = 1420 eV, E$_{kin}$ = 570 eV) corresponds to an information depth of approximately 3 nm,[27] only a fraction of the NPs volume can be characterized. These results are however consistent with the bulk characterization performed by Raman spectroscopy, where only the Ni_2.5x1.5y sample (Figure S2)

4

shows the vibration breathing mode typical of Ni-P bonds. The analysis of the satellites provides additional information: for Ni_5x1.5y, the satellite relative to the metallic component N1 was found with an area of 35% of the main peak, which is consistent with results in the literature;[26a] moreover, the satellite component relative to the Ni phosphide phase at 860.5 eV in Ni_2.5x1.5y is indeed 15% of the main peak, as it was found for a phosphorous enriched Ni_2P phase.[26a]

Another difference amongst the samples is the ratio between the components contributing to the core of the NPs (Ni1 metallic and Ni4 Ni-P components) and the those relative to the oxy-hydroxide layer at the interface with the organic shell (Ni2 and Ni3). Particularly, the higher intensity of the components of the Ni_2.5x1.5y core would be an indication of a thinner organic shell, which enables to probe a larger volume of the metallic core. Also, the smaller clusters embedded within the organic shell of Ni_5x1.5y and of Ni_10x1.5y, which are apparently absent in Ni_2.5x1.5y, might be fully detected within the probing depth of these measurements, as opposed to the main NPs' core, which is only partially characterized. This explain the higher abundance of the surface components in Ni_5x1.5y and in Ni_10x1.5y. [28] This reasoning is also confirmed by the Ni/C ratio as determined by XPS quantification which was found to be 2.2, 1.4 and 0.4 for the Ni_2.5x1.5y, Ni_5x1.5y and Ni_10x1.5y. respectively.

The spin-orbit split Ni L-edge absorption spectra of these samples in Figure 4d present the L_3 and L_2 resonances maxima of Ni(0) at 852.6 eV and 870.2 eV, respectively,[29] whereas in nickel oxide they are reported to be at 853.2 eV ($2p_{3/2}3d^9$) and 870.3 eV ($2p_{1/2}3d^9$).[8b,30] However, compared to the spectra reported in literature for Ni metal, the NPs characterized in this study show broadening of the L_3 and L_2 resonances towards higher photon energies. According to Watson and co-workers,[8b] this broadening is a result of the greater contribution of a surface oxide layer formed under ambient conditions. The most striking difference amongst the spectra reported here is the shift of the main resonance to higher photon energy, by about 0.5 eV, and the significant broadening to the high energy side of the Ni_2.5x1.5y sample. Similar results were found for Ni phosphides,[26a] which is indicative of the partially cationic character of Ni in these compounds, where the higher the P content, the higher the energy shift.

We thus conclude that the reduction of the Ni^{2+} precursor to Ni^0 by the action of OAm and formation of crystalline Ni NPs occurs below the temperature of the TOP decomposition. Similar conclusions have been reported elsewhere.[31] However, if the amount of OAm is lower than the quantity needed to reduce quantitatively the Ni^{2+} precursor, as in the case of Ni_2.5x1.5y, the molecules of the TOP capping agent will coordinate to the Ni complex in excess in solution. Only when the TOP decomposes at the maximum temperature reached in these experiments (220 °C), the amorphous Ni phosphide particles are formed. The presence of hollow NPs in Ni_2.5x1.5y suggests that the Ni phosphide phase can be formed *via* phosphidation of the initially formed Ni^0 nuclei.[31]

Structural characterisation of SiO_2-supported Ni NPs

In the case of supported NPs, the NPs were first synthetized and subsequently immobilized onto the silica support. We used 5 equivalents (x) of OAm and investigated how changing the

amount of protective agent TOP (y) influences the nanostructure of the Ni NPs. The same range of OAm: TOP ratios were investigated as in the case of the unsupported NPs. In the subsequent immobilization step, the metal loading was kept low to facilitate the NPs' dispersion on the support. The metal loadings on these samples determined by EDX confirm the quantitative immobilization of the preformed NPs onto the support (table S1 of the supporting information). While for Ni/SiO₂_5x1.5y and Ni/SiO₂_5x3y the HAADF-STEM images in Figure S4 show the expected nanoparticulate morphology, the Ni/SiO₂_5x0.75y sample shows a cauliflower-like morphology as a result of the low amount of capping agent used, whose role is also to facilitate nuclei agglomeration and sintering.
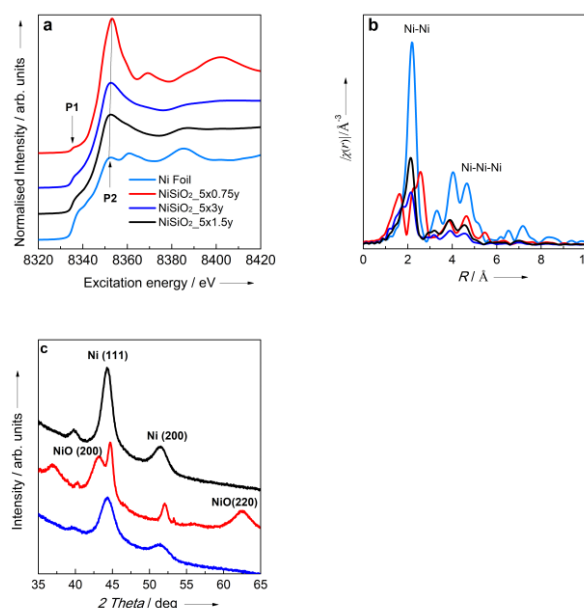

Figure 5. Ni K edge XANES (a) and EXAFS (b) in transmission mode; XRD characterization of the samples(c). Colour code: Ni/SiO₂_5x1.5y (black line); Ni/SiO₂_5x3y (blue line); Ni/SiO₂_5x0.75y (red line).

Due to the SiO_2 component of these materials making the spectroscopic structure analysis by means of electron detection challenging, the electronic structure of the supported samples was investigated by bulk-sensitive XANES and EXAFS at the Ni K-edge in X-ray transmission mode. The samples are compared with a nickel standard (Ni foil) in Figures 5a and 5b, respectively. The XANES spectra exhibit two relevant features: the peak P1 at *ca.* 8336 eV corresponding to either the quadrupole transitions of 1s photoelectrons to Ni3d–O2p hybridized orbitals for the oxide phase or the edge for the metallic phase or a combination of both; the peak P2 at 8352 eV corresponding to transitions of 1s to Ni4p–O2p orbitals[32] for the oxide phase. With respect to the Ni foil, Ni/SiO₂_5x1.5y and Ni/SiO₂_5x3y clearly show a less intense pre-edge region P1 and a more intense P2 peak. The position of the K-edge (defined as the position of maximum first derivative) was previously found for Ni phosphides between NiO and Ni standards, indicating that the formal oxidation state for phosphides ranges between 0 and 2, where the higher the amount of P, the higher the energy position of the edge.[33] However, the spectra of these samples (Figure

5a) do not show significant edge-shifts but rather a systematic increase of the peak P2 intensity and correspondingly a decrease of the P1 resonance. P2 is significantly pronounced in the Ni/SiO$_2$_5x0.75y spectrum, resembling XANES spectra of NiO reported in the literature.[26,33] Based on this, we propose that the samples are composed of a mixed Ni oxide and metallic phases, whereby spectral variations amongst the samples account for changes in composition of the two phases. Although a Ni phosphide phase cannot be completely excluded, its contribution should be negligible. The absence of the Ni-P signature in the Raman spectra of the samples (not shown) corroborates this assumption. If we assume that the oxide component is a surface overlayer of the metallic core, the measured increase in the P2 feature corresponds to a higher fraction of NiO and therefore to smaller particles size. [34]

Table 2. XANES Linear Combination Fit and EXAFS fit				
XANES[a]	**Ni(0)**	**NiO**	**R-factor**	**Red. χ^2**
NiSiO$_2$_5x1.5y	0.61	0.39	0.005202	0.00063
NiSiO$_2$_5x0.75y	0	1.	0.007883	0.001398
NiSiO$_2$_5x3y	0.48	0.52	0.006709	0.000847
EXAFS[b]	**Ni(0)**	**NiO**	**R-factor**	**Red. χ^2**
Ni/SiO$_2$_5x1.5y	0.53	0.47	0.032123	3614.764
Ni/SiO$_2$_5x0.75y	0.2	0.8	0.05524	6511.449
Ni/SiO$_2$_5x3y	0.50	0.5	0.030047	1175.56
[a] Linear Combination Fit using Ni metal and NiO as references. [b] EXAFS fit using combination of two models: Ni-Ni scattering paths for metal and Ni-O scattering paths for oxide and a variable ratio between the two.				

To prove our assumption, we perform a linear combination fit of the XANES spectra using Ni metal and NiO as standards, which also enabled a quantitative analysis of the two phases, as summarized in Table 2.

The Fourier transforms of the Ni K-edge EXAFS spectra are presented in Figure 5b. The standard nickel foil is also included for comparison. The first peak in face-centered cubic (fcc) Ni is found at 2.48 Å, which is also found in the Ni/SiO$_2$_5x1.5y and 5x3y samples, although with attenuated intensity, while it is barely visible in 5x0.75y. The peaks at higher distances correspond to main single scattering paths of metallic Ni-Ni higher coordination shells (at 3.50, 4.29, 4.96 Å respectively). In the EXAFS spectra of Ni/SiO$_2$_5x0.75y, other peaks assigned to single scattering of Ni-O (2.09 Å) and Ni-Ni (2.96 Å) in nickel oxide are clearly visible, indicating that this is the predominant phase in this sample. The EXAFS data are fitted for a quantitative interpretation and reported in Table 2. The results of the fit confirm the trend observed for the XANES linear combination fits. Moreover, in the radial distribution function for the Ni/SiO$_2$_5x3y sample, only the first shell peak is observed, while other samples also show the Ni-Ni higher coordination shell. This means that the Ni/SiO$_2$_5x3y sample is only short-range ordered. This is also confirmed by the fact that the obtained Debye-Waller factors from the fit is much higher for all shells (σ$^2_{1st\ shell}$ = 0.011 vs. 0.008, σ$^2_{higher\ shells}$ = 0.0243 vs. 0.0140).

Furthermore, we note that previous literature on Ni phosphides has indicated that the radial distribution function presents pronounced changes with the content of P and that the FT EXAFS of the Ni/SiO$_2$_5x3y sample is similar to the spectrum reported for a Ni$_{12}$P$_5$ phase with a calculated oxidation state of 0.43.[33-34] Therefore, it could also be possible that the Ni/SiO$_2$_5x3y sample might contain a small amount of P as an amorphous phase.[35] This could be expected considering that the OAm:TOP ratio used in its synthesis was similar to the one used in the preparation of the unsupported Ni _2.5x1.5y sample. However as discussed above, the Ni phosphide phase can be safely neglected in this data treatment.

X-Ray diffraction was used to investigate the structure and phase composition of the samples and to calculate the mean NPs size. Figure 5c compares the XRD patterns of the three supported samples between 35 and 65 degrees 2θ. Similarly to the unsupported NPs, the Ni/SiO$_2$_5x1.5y and Ni/SiO$_2$_5x3y samples show the characteristic peaks at 44.4 and 51.7 degrees 2θ, which correspond to the nickel (111) and (200) reflections, respectively.[18] Only the Ni/SiO$_2$_5x0.75y sample shows a mixture of Ni$^{(0)}$ and fcc NiO phases (NiO (111), (200) and (220) reflections at 37.0, 43.2 and 62.5 degrees 2θ, respectively).[36] Moreover, the diffractograms do not show reflections reported for crystalline Ni phosphides. Instead, broadening of the main peak indicates a smaller crystallite size.

While trends in the crystallite size calculated from the XRD data for the 5x1.5y (4.7 nm) and 5x3y (3.8 nm) samples are in agreement with what can be imaged by STEM (5x1.5y particles are larger than 5x3y) as summarized in Table 1, the absolute value is very different. Moreover, there is an apparent discrepancy for the Ni/SiO$_2$_5x0.75y sample. The Ni/SiO$_2$_5x0.75y sample shows sharp Ni reflections whereby the mean crystallite size was calculated to be 7.3 nm. Whilst these peaks are sharper in the Ni/SiO$_2$_5x0.75y sample than in the other samples, its main phase is likely to be NiO. The estimated crystallite size for the NiO phase from XRD is around 2.5 nm. However, STEM images clearly show that the catalyst consisted of particles that are much smaller than the other two samples, with a particles size consistent with the size of NiO phase determined by XRD. We therefore propose that for the Ni/SiO$_2$_5x1.5y and Ni/SiO$_2$_5x3y a large fraction of the NPs is in XRD-amorphous state or twinned NPs with coherent size of the twins as determined by XRD, whereas for the Ni/SiO$_2$_5x0.75y, the large Ni crystallites are covered by smaller oxide NPs forming the cauliflower-like morphology seen in the HAADF-STEM image (Figure S4).

Similarly to the unsupported NPs, the size and the structural characteristic of the supported nanoparticles can be rationalized taking into account the synthetic conditions and the systematic variation of the x:y ratio. When comparing the Ni/SiO$_2$_5x3y and Ni/SiO$_2$_5x1.5y samples, as the number of TOP equivalents (y) is increased, the size of the nanoparticles is reduced, since the growth step is further hindered by relatively more abundant capping agent.[19,37] We explain the peculiar morphological and structural characteristics of the Ni/SiO$_2$_5x0.75y sample by taking into account the current opinion in the synthesis of NPs.[38] Accordingly, in the relative excess of the reducing agent (oleylamine), a large number of metal nuclei are formed; these, assisted by TOP, are prone to growth or agglomeration during the high temperature reaction, forming a small amount of relatively bigger Ni^0 NPs. However, it is reasonable to assume

6

that with low concentration of TOP (y<1), the nanoparticles being formed in the high temperature reduction of Ni(acac)$_2$ with OAm are not all being encapsulated by TOP thus remaining not sufficiently protected from oxidation upon exposure to the environment. The peculiar cauliflower-like morphology of the main oxidic crystallites in the sample also suggests that TOP favors the packing of the small NPs to form bigger twinned NPs.

Catalytic performances of the synthetized unsupported and SiO$_2$-supported NPs.

Table 3. Catalytic performance of TA modified Ni NPs in hydrogenation of methyl acetoacetate. [a]

Samples	Tot. MAA conv. (%)[b]	Inst. (*R*)-MHB selec. (%)[c]	Final *ee* (%)[d]
Ni_5x1.5y	69	48	–3
Ni_2.5x1.5y	36	48[e]	–3
Ni_10x1.5y	74	46	–4
Ni/SiO$_2$_5x0.75y	7	62[f]	24
Ni/SiO$_2$_5x3y	3	48[g]	7

[a] Reaction conditions: 0.5 g of unsupported NPs or 1 g of Ni/SiO$_2$. MAA (0.15 mol), MeOH solvent (15 mL), H$_2$ 20 bar, T 60 °C. [b] Conversion after 22 h of reaction. [c] Unless otherwise stated, selectivity at the same value (50%) of total MAA conversion. [d] Positive values indicate (*R*)-selectivity, negative (*S*)-selectivity. [e] Value at 36% conversion. [f] Value at 7% conversion. [g] Value at 3% conversion.

The synthetized NPs were tested in the enantioselective hydrogenation of MAA. Before the catalytic tests, the NPs catalysts were pretreated with (R,R)-TA and NaBr following a modification procedure which proved to be effective in chemisorbing TA on the surface of polycrystalline Ni. The analysis of the surface chemical compositions upon various modification procedures was afforded by XPS characterization and revealed a very complex chemical speciation which was significantly affected by the experimental conditions. It is thus expected that the surface chemical composition of the reactive interface of the catalyst changes dynamically under hydrogenation conditions. A more detailed discussion is reported in the supporting information (Figure S5). The combined NaBr and TA modification was also confirmed to enhance the enantiomeric selectivity towards the (R)-MHB as well as the activity in the case of Raney Nickel (Table S2), consistently with the literature. [1, 13]

The chirally modified NPs produce both (*R*)-MHB and (*S*)-RHB (Figure 6). No other product was observed under the experimental conditions used.

Table 3 summarizes the catalytic performance of the supported and unsupported nanoparticles in the hydrogenation of MAA. The final enantiomeric excess (*ee*) is calculated according to equation (1), given the concentration of (*R*)-MHB and (*S*)-MHB at the end of the reaction; where possible, the instantaneous selectivity towards (*R*)-MHB is compared at the same value (50%) of total MAA conversion, thus the values reported here are extrapolations from the fits presented in Figure 6.

As it can be seen from table 3, the activity (total MAA conversion) of the unsupported Ni_5x1.5y and Ni_10x1.5y

samples at 22h of reaction did not vary significantly, indicating that there is no size-effect on the activity at this reaction time and at such variations of the crystalline domains (4.0 nm *vs*. 5.6 nm from XRD); in contrast, the activity of the Ni_2.5x1.5y was significantly inferior (36% tot. conv.). Note that the as prepared sample is composed of large particles of average diameter of 8 nm composed of a predominantly amorphous Ni phosphide phase whereas the size of metallic crystallites is much smaller (1.3 nm circa in table 1).
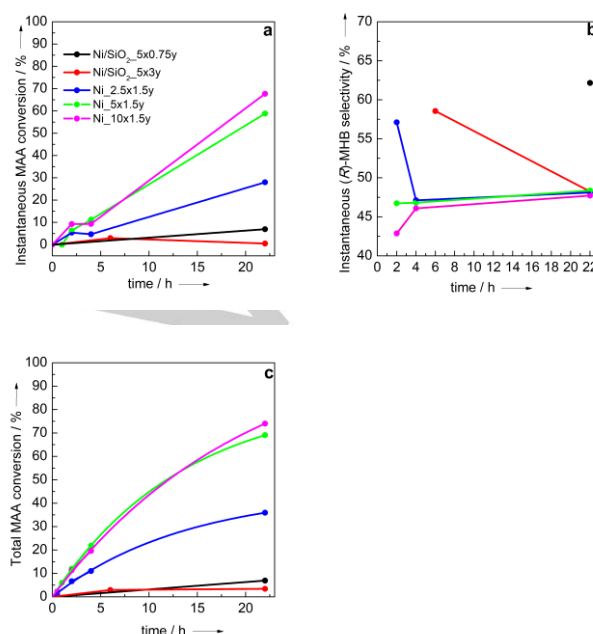

Figure 6. Instantaneous conversion of MAA *vs*. time of reaction (a) and corresponding selectivity to (*R*)-MHB (b). Total conversion of MAA (c).

Figures 6a and 6b report the instantaneous conversion of MAA and selectivity as a function of the reaction time for the unsupported and SiO$_2$-supported NPs, respectively. The total conversion of MAA as a function of reaction time is reported in Figure 6c. With respect to the total conversion and selectivity, the instantaneous conversion and selectivity provide a direct evaluation of changes in the catalytic performances as well as deactivation. Indeed, we can observe that the activities of the catalysts are steadily increasing for the unsupported Ni NPs. This is an indication that the chemisorbed species composing the surface overlayer detach from the Ni surface with time and as a consequence new surface is exposed during the reaction, which is now available for catalysis.

However, the increase of the activity is not reflected in an increase of the selectivity towards the (R)-MHB. Particularly, for the unsupported Ni_5x1.5y and Ni_10x1.5y the selectivity towards the (R)-MHB is maintained constant within the time frame investigated regardless of the MAA conversion achieved.

Interestingly, we observe for the unsupported Ni_2.5x1.5y that at the beginning of the reaction the selectivity towards the (R)-MHB is higher but decreases very rapidly to reach the value of circa - 3% *ee*. This value seems to be characteristic for these unsupported NPs systems, in which we postulate that the chiral modification is no longer presents.

7

In general, the measured activities for the SiO₂-supported Ni NPs samples were very poor with a very low conversion, in part due to the low loading of Ni (10% in weight) in these catalysts. However, at such a low conversion, the Ni/SiO₂_5x0.75y sample shows an ee of 24%, which is the highest *ee* towards (*R*)-MHB observed in this study and similar to the one obtained for Raney Ni modified using the same procedure (Table S2). Similarly, the selectivity of Ni/SiO₂_5x3y towards (*R*)-MHB is initially high but decreases with time.

Figure 7 shows BF-STEM and HAADF-STEM images of the Ni_2.5x1.5y after the reaction. LM images of the same sample are reported in Figure S5. It is worth noting that, despite the core-shell structure still being present, the core of the NPs is now clearly crystalline whereas the shell is much thicker. Interestingly, the shell is now composed of more abundant crystalline nano-clusters covering the overall surface and, imparting a much rougher aspect to the surface shell structure (Figure 7). This clearly indicates that Ni NPs, which are initially in the Ni-P amorphous phase, undergo structural changes towards the formation of a more crystalline Ni over-layer during the hydrogenation reaction.

Raman spectra of the Ni_2.5x1.5y after 22 h of reaction suggest that the sample is highly inhomogeneous in character (Figure S6). The five spectra taken at different spots were quite different, with two exhibiting a weak peak at *ca*. 600 cm⁻¹, suggesting that a small amount of Ni phosphide phase may now only be present in certain regions of the sample. However, these structural characteristics seen in Figure 7 are not enabling enantiomeric differentiation.
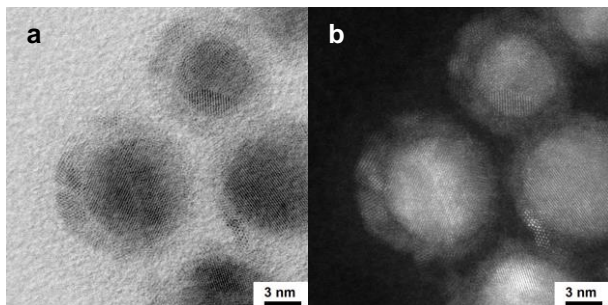

Figure 7. BF-STEM images (a) and corresponding HAADF-STEM (b) of Ni_2.5x1.5y after 22 h of hydrogenation reaction.

Correlation between catalytic performances and structural characterization

The comparative analysis of the reactivity data of the unsupported samples shows that large metal crystallites lead to higher conversion. In contrast, the enantio-selectivity is mainly unaffected by the size of the NPs. Higher initial value of selectivity towards the (*R*)-enantiomer was obtained on the Ni 2.5x1.5y catalyst, which contains cationic Ni species in the form of a phosphide. However, the selectivity for (*R*)-MHB reached a similar value for all unsupported catalysts after 22h of reaction.

The measured activities for the supported samples were generally very poor (Figure 7b). This is only in minimal part due to the low loading of Ni (10% in weight) in these catalysts. Indeed, the Ni/SiO₂_5x0.75y sample, which was initially present predominantly as a NiO phase, shows a particularly low

conversion of 7% after 22h of reaction, probably due to the slow reduction to form the active hydrogenation Ni⁰ phase. Interestingly, in this condition, the catalyst shows the highest *ee* towards (*R*)-MHB observed in this study (23%).

Indeed, in this study we could identify that high selectivity towards (*R*)-MHB is obtained when a cationic Ni phase is present (NiO for the supported or NiP for the unsupported).

It is generally observed that (*R*)-MHB is favored when (*R*,*R*)-tartaric acid is used as modifier together with NaBr and was confirmed in this work also for Raney Nickel investigated under the same reaction conditions (Table S2).

The observation of enantioselective differentiation for some of the catalysts at the beginning of the reaction further confirms that during the *ex situ* modification step with (*R*,*R*)-tartaric acid and NaBr, some level of exchange of the capping agents with the chiral modifier takes place as also proved by the XPS in Figure S5 for polycrystalline Ni. However, the fact that the instantaneous conversion increases steadily with time whereas the selectivity at higher conversion is maintained at the value of the racemic composition indicates that the capping agent was not quantitatively substituted by TA and NaBr.

In fact, as the achiral capping agent detaches from the round shaped NPs, the amount of left and right kinks sites or left and right planes is equal and thus a macroscopically achiral metal surface is freed. [1] At this point, the selectivity reaches the value which is characteristic of an unmodified Ni⁰ surface.

Moreover, we suggest that the lack of enantiomeric differentiation of the Ni_5x1.5y and Ni_10x1.5y is the result of the weak chemisorption of the chiral molecule on the Ni metallic surface which desorb easily from the Ni surface upon hydrogenation conditions, where the dynamic surface diffusion of metal atoms and restructuring typical for NPs [28] results in an inefficient chiral modification. The weak chemisorption of TA on metallic Ni was also proved for the case of polycrystalline Ni reported in the supporting information (Figure S5).

Thus, from the catalytic data presented here, it may be assumed that the mechanism that involves the formation of a chiral arrangement of TA molecules on flat Ni surfaces, leaving a chiral imprint on it upon TA desorption[39] is the least probable mechanism to explain the chiral action of TA and NaBr in these nanoparticulate systems. The higher enantiomeric selectivity at low reaction times on oxidized samples can be correlated to the higher chelating affinity of the carboxylate species of the TA-Na towards cationic Ni. As discussed in previous literature, [9-10] TA is highly corrosive and Ni²⁺ species coordinated to TA can leach out leaving (R)-kinks behind. However, whilst we cannot role this mechanism out, we would have expected that the rapid dynamic restructuring of these (R)-kinks sites would not allow us to be able to measure such a transient and short-lived enantiomeric differentiation similarly to the case of the metallic NPs Ni_5x1.5y and Ni_10x1.5y. We therefore suggest that the most probable mechanism that describes our results involves strongly chemisorbed TA on the surface of oxidized Ni. Indeed, TA binds more strongly on NiO than on Ni metal, and under hydrogenation conditions prevents its reduction. However, on adjacent unprotected reduced Ni⁰, which is the active phase for the hydrogenation, TA can assist the favorable chemisorption of MAA to form (*R*)-MHB. This is consistent with previous work on the adsorption of tartaric acid and MAA on Ni surfaces.[7] Particularly, a hydrogen bonding interaction between the hydroxyl of a TA molecule chemisorbed via the two carboxylates

8

on Ni[7] and the ester-oxygen of a MAA molecule chemisorbed via the ester-carbonyl might occur. This intermolecular interaction of the chemisorbed species constrains the interaction of the MAA through the ketone carbonyl with the chemisorbed H atoms on the Ni from the side that leads to the (R)-enantiomer formation. However, with time, the NPs is reduced, under hydrogenation and simultaneously TA will detach more easily from the surfaces of the NPs leaving achiral NPs.

Conclusions

In this work, we have synthetized Ni NPs and SiO$_2$-supported Ni NPs obtained *via* hot-injection using different ratios of reducing and capping agents and characterized the morphology, nanostructure and chemical composition. Size and phase control during synthesis was revealed together with the impact of these characteristics on the resulting catalytic performance in the selective enantiomeric hydrogenation of MAA. Our findings imply that the more likely role played by the modifier under the conditions investigated is not to generate the chiral Ni surface, but rather to be involved in a chemical interaction with the pro-chiral substrate, thus assisting a specific configuration of chemisorption of the latter on the metallic Ni active surface that leads to the selective (R)-enantiomer formation.

It is therefore evident that to design highly active and (R)-selective hydrogenation catalysts, a combination of large Ni metallic surface domains is needed, together with the existence of Ni cationic islands where the chiral modifier can strongly chemisorb to assist the side-by-side selective hydrogenation of MAA. We speculate that, at an optimal concentration, sodium bromide plays a similar role, whereas an excessive amount could act as irreversible poison of the catalyst surface.

Experimental Section

Materials and Methods

The synthesis of both unsupported and silica-supported nickel nanoparticles *via* thermal decomposition reduction method was adapted from the literature.[20b] Oleylamine (OAm, x) was used
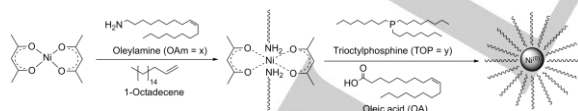
as reducing agent whereas trioctylphosphine (TOP, y) and oleic acid were used as capping agents.

Scheme 2. Hot injection synthesis of monodisperse NPs. Adapted from ref.[15b]

The amount of oleylamine or TOP was varied as a strategy to tailor the particle size, as described in Table 1. The total number of equivalents of OAm and solvent (1-octadecene) was kept constant (21 molar equivalents), therefore the volume of solvent was also systematically varied. All other parameters (concentration of nickel precursor, temperature, and oleic acid, reaction time) were not varied. Reaction yields (mass of isolated

NPs with respect to number of moles of Ni precursor) were typically between 70% and 80%.

List of reagents Technical grade nickel(II) acetylacetonate (95%), oleylamine (70%), trioctylphosphine (90%) and 1-octadecene (90%) reagents were purchased from Sigma-Aldrich and used as received without further purification. Oleic acid (≥ 99%, GC grade), L-(+)-tartaric acid (ACS reagent, ≥ 99.5%), anhydrous sodium bromide (ACS reagent, ≥ 99%) and methyl acetoacetate (ReagentPlus®, 99%) were also purchased from Sigma-Aldrich and used as received. CAB-O-SIL® (M-5 scintillation grade, 200 m^2/g) was purchased from Acros Organics (Fisher Scientific) and used as received. Polycrystalline nickel discs (10 × 1.5 mm) were sourced from *Goodfellow Cambridge*. Raney Ni was purchased from *Sigma Aldrich*.

Unsupported NPs – variation of x (OAm) number of equivalents
Reactions were carried out under an atmosphere of high-purity argon to protect nickel and trioctylphosphine from oxidation; the temperature was controlled with a thermocouple placed directly inside the reaction vessel. In a typical synthesis, Ni(acac)$_2$ (3.46 g, 13.45 mmol) and oleylamine (22.13 mL, 67.27 mmol) were mixed together in 68.87 mL of 1-octadecene and stirred magnetically at 65-70 °C in a flow of Ar under reflux conditions. Once the mixture was completely dissolved, trioctylphosphine (9 mL, 20.18 mmol), after having been degassed with nitrogen for 10 minutes, was rapidly injected into the flask, followed by re-setting the temperature to 120 °C and holding it for 10 minutes. The mixture was then rapidly heated to 220 °C over the course of 15 minutes for nucleation and ripening of the nanoparticles. After 2 hours of reflux, the synthesis was halted and the flask cooled to room temperature. Oleic acid (1.35 mL, 4.25 mmol) was then added to the mixture, followed by ultra-sonication for 10 minutes. The nickel nanoparticles were then precipitated by adding anhydrous ethanol (150 mL) and centrifuging the dispersion at 8500 rpm for 30 min. The wet catalyst was then suspended in a mixture of hexane (10 mL) and anhydrous ethanol (30 mL) and centrifuged for a further 30 min at 8500 rpm. This process was repeated twice.

Supported nanoparticles – variation of y (TOP) number of equivalents
In the case of supported catalysts, the protocol above was followed but, instead of precipitating the NPs *via* treatment with a poor/good solvent mixture (ethanol/hexane) and centrifugation (flocculation method), they were supported on silica (CAB-O-SIL 5M). Amounts of Ni(acac)$_2$ precursor, OAm, TOP, 1-octadecene and SiO$_2$ support were adjusted to obtain *ca.* 4 g of sample with a theoretical NPs loading of 10 wt% (assuming 100% reduction yield and 100% incorporation of nanoparticles on the support). To achieve the impregnation of the nanoparticles on silica, CAB-OSIL 5 M was first dispersed in absolute ethanol (150 mL); under vigorous stirring, the reaction mixture was added to the support dispersion, which was then filtered under suction and washed multiple times with copious EtOH until the runnings were essentially colourless, indicating removal of excess surfactants.

Ex situ modification with tartaric acid
All nanoparticulate systems and the Raney Nickel catalysts were subjected to *ex situ* modification with (R,R)-tartaric acid (TA). The catalyst (0.5 g of unsupported NPs, 1 g of Ni/SiO$_2$ sample) was refluxed at 100 °C for 1 h in 100 mL of the modification solution (1 wt% TA, 20 wt% NaBr co-modifier, pH 5.1 adjusted with 1 M NaOH), followed by washing with one portion of water (50 mL) and 2 × 25 mL portions of

9

methanol. Prior to modification, the supported nanoparticles were treated under a stream of 10% hydrogen gas in He gas at 300 °C for 1 h. The samples were then cooled to r.t. under N_2 before the modification solution was injected into the vessel, thus avoiding exposure to air.

Other samples were obtained starting from Raney Ni, which was modified in an aqueous solution containing either only 20 wt% NaBr or 1 wt% TA, following the same procedure as indicated above.

Ex situ modifications of polycrystalline Ni for XPS analysis

The Polycrystalline Ni discs were first reduced under a constant steam of 5% H_2 in He in a tube furnace at 450 °C for 16 h before being stored under Millipore water for transport to minimise contact with atmospheric O_2. Following, the discs were subjected to chemical modifications using a Schlenk line. 2 discs were transferred into each modifying solution; (1) 150 mL of Millipore H_2O for the unmodified sample; (2) 1.5 g of TA in 150 mL of Millipore H_2O; (3) 30 g of NaBr in 150 mL of Millipore H_2O; (4) 1.5 g of TA and 30 g of NaBr in 150 mL of Millipore H_2O. Millipore water used in these experiments was either degassed under vacuum prior to being used (1 and 2) or boiled under N_2 for 30 min before being used (3 and 4). Solution 1 containing the discs was not refluxed, while solutions 2 – 4 were refluxed under N_2 for 1 h.

After refluxing, a disc was removed from solutions 2 - 4 and rinsed with Millipore water and stored under N_2 degassed water for at least 60 h. The samples were then mounted on sample holders under water before being placed in the load lock to pump away the water. X-ray photoelectron spectroscopy (XPS) spectra were then taken of the Ni 2p, O 1s, C 1s and Valance Band regions.

Catalyst characterisation

The supported and unsupported NPs were characterized prior to exposure to H_2 and *ex situ* modification with tartaric acid.

X-ray powder diffraction measurements were carried out on a Rigaku Miniflex 600 diffractometer, using CuKα radiation. A silicon NIST SRM 640e standard sample was firstly measured, in order to obtain the instrumental resolution function of the diffractometer. The obtained diffraction pattern for each sample was Rietveld refined using TOPAS 5 software[40] and the corresponding crystallite sizes were estimated by using calculated integral breadth-based volume-weighted column heights[41] assuming monodisperse spherical systems of particles.

X-ray absorption fine structure spectra at the Ni K-edge were obtained from experiments at the B18 beamline in Diamond Light Source, UK.[42] The measurements were carried out using a fixed-exit double-crystal Si(111) monochromator and the Pt-coated branch of collimating and focusing mirrors. Harmonic rejection mirrors were placed in the beam path and used as a low-pass filter to remove higher energy harmonics. The beam size at the sample position was approximately 1x1mm. All samples were prepared in forms of pellets (13 mm diameter) mixing 50 mg of sample with 50 of cellulose to optimize the edge jump and total transmission. The measurement was performed at room temperature in transmission mode using 3 ion chambers filled with following gases: 300 mbar N_2 + 700 mbar He (I0); 150 mbar Ar + 850 mbar He (I1, I2). The spectra were collected in quick EXAFS mode by continuously scanning the monochromator with a constant energy step size of 0.3 eV. The scan covered an energy range from 8133.15 to 9333 eV, corresponding to a k-range of 16Å^{-1}. For each sample, 3 scans were acquired and subsequently merged to improve the signal to noise ratio. Data were normalised using the program Athena[43] with a linear pre-edge and 2nd order polynomial post-edge. After background subtraction, the resulting $\chi(k)$ functions were k^2-weigthed and Fourier transformed in a range from 2 to 15.5 Å^{-1}. The EXAFS fit was performed using the two references

structures, Ni^0 and NiO, for which the most relevant single and multiple scattering paths were calculated. The amplitude of each signal was then described as a function of the ratio of the phases generating the scattering path and the ratios optimized during the fit of the experimental data.

X-ray photoelectron spectroscopy (XPS) and near edge X-ray absorption fine structure (NEXAFS) measurements in the soft X-ray regime were carried out at the VERSOX end station and beamline at the UK synchrotron facility Diamond Light Source. The freshly prepared samples from atmospheric environment were deposited on a Si wafer and directly exposed to vacuum (10^{-8} mbar) in the XPS chamber. XPS measurements were performed by applying a suitable excitation energy corresponding to a kinetic energy (KE) of the photo-emitted electrons of 450 eV for the core levels Ni2p, C1s and O1s. The energy pass Ep was normally set to 20 eV. The core levels envelopes were fitted using Casa XPS software after subtraction of a U2 Tougaard background.

The fittings of the Ni2p spectra were performed by considering four core-level components. A DS function line-shape was used for both the metallic Ni1 and phosphide Ni4 components whereas two components with a Gaussian-Lorentzian (GL) line-shape (Ni2 and Ni3) were included accounting for Ni^{2+} and Ni^{2+}/Ni^{3+} oxyhydroxide components, respectively. The fitting of the spectra was done by constraining the peak position by ± 0.05eV. The peak area ratio between the Ni2p$_{3/2}$ and Ni2p$_{1/2}$ spin orbit split transitions was constrained approximately to the theoretical value of 2:1 and the distance between the two-spin orbit split transition was 17.2 eV. Binding energies (BEs) were referenced to the maximum of the C1s core level peak (284.3 eV) measured after every other core level measurement at the corresponding excitation energy. The satellite feature for Ni^0 is 5.7 eV upshift with respect to the core level, whereas its intensity is 35% of the main peak.

Auger Electron Yield (AEY) NEXAFS spectra were recorded with an analyser setting of 50 eV pass energy (Ep) and electron kinetic energy (KE) of 700 eV, 520 eV and 240 eV for Ni L, OK and CK, respectively. The beam-line setting was 0.5 μm x 0.04 μm exit slit (ES) and fix focus constant (cff) 2.0 (cff = cosα/cosβ).

Bright field (BF) and high angle annular dark field scanning transmission electron microscopy (HAADF STEM) images were acquired on a probe corrected ARM200F at the ePSIC facility (Diamond Light Source) equipped with a cold-FEG and operated at an acceleration voltage of 200 keV enabling a resolution of 0.78Å. Measurement conditions were a CL aperture of 30 μm, convergence semiangle of 24.3 mrad, beam current of 12 pA, and scattering angles of 0-10 and 35-110 mrad for BF and HAADF STEM respectively. Samples were deposited onto 3mm holey carbon Cu- grids for TEM analysis.

Raman spectroscopy experiments were performed using 532 nm laser excitation and a conventional single grating (1200 lines per mm) 0.32 m Raman spectrometer. The spectra were calibrated using the intense phonon mode in Si at 520.0 cm^{-1}, and the spectral resolution was verified to be at worst 3.2 cm^{-1} half width half maximum. The notch filters on the spectrometer allowed collection of data down to 270 cm^{-1}. This was verified by the observation of a radial breathing mode peak from a single-walled carbon nanotube sample centered on this wavenumber.

Hydrogenation reaction of MAA under batch conditions

The modified Ni catalysts were then tested for the hydrogenation reaction of methyl acetoacetate (17.0 g, 0.15 mol) in methanol (15 mL) using a batch reactor at a working H_2 pressure of 20 bar, temperature of 60 °C,

10

with stirring set to 750 rpm. 0.5 g of unsupported NPs and 1 g of supported NPs were used for the catalytic tests. Samples of the solution were taken over a period of 22 h, filtered to remove any solid catalyst and prepared for GC analysis (500 μL mixed with 10 μL of decane). Shimadzu GC 2014 with FID and Shimadzu AOC-20i autosampler attachment were used for experimental analysis, in combination with a Supelco Analytical Beta Dex 325 capillary column. From the chromatographs, the concentration of each species x was calculated from the concentration of the internal standard (IS, decane), the detector response factor (DRF) of each analyte x, and the peak area of analyte and IS (A_x and A_{IS}), as shown in equation (2). Catalytic data were then calculated from the concentrations of MAA, (*S*)-MHB and (*R*)-MHB. The instantaneous conversion of MAA and the instantaneous selectivity towards the (*R*)-enantiomer with respect to the products were calculated as given in equations (3) and (4). Exponential and linear equations were used to fit the conversion and selectivity data, respectively. Equation (5) was used to calculate the total conversion of MAA and an exponential function was used to fit the data (Figure S4).

$$ee\ (\%) = \frac{[(R)-MHB] - [(S)-MHB]}{[(R)-MHB] + [(S)-MHB]} \times 100 \tag{1}$$

$$[x] = \left(\frac{A_x}{A_{IS}}\right) \times \left(\frac{[IS]}{DRF}\right) \tag{2}$$

$$\text{Inst. MAA conv. (\%)} = \frac{([MAA]_{t-1} - [MAA]_t)}{[MAA]_{t-1}} \times 100 \tag{3}$$

Inst. (*R*)-MHB selectivity (with respect to products) (%) =

$$\frac{([R-MHB]_t - [R-MHB]_{t-1})}{[([R-MHB]_t - [R-MHB]_{t-1}) + ([S-MHB]_t - [S-MHB]_{t-1})]} \times 100 \tag{4}$$

$$\text{Total MAA conv. (\%)} = \frac{([MAA]_0 - [MAA]_t)}{[MAA]_0} \times 100 \tag{5}$$

Acknowledgements

[1]   a) T. Mallat, E. Orglmeister, A. Baiker, *Chem. Rev.* **2007**, *107*, 4863-4890; b) G. Kyriakou, S. K. Beaumont, R. M. Lambert, *Langmuir* **2011**, *27*, 9687-9695; c) F. Meemken, A. Baiker, *Chem. Rev.* **2017**, *117*, 11522-11569.
[2]   Y. Izumi, in *Advances in Catalysis, Vol. 32* (Eds.: D. D. Eley, H. Pines, P. B. Weisz), Academic Press, **1983**, pp. 215-271.
[3]   T. J. Blacklock, P. Sohar, J. W. Butcher, T. Lamanec, E. J. J. Grabowski, *J. Org. Chem.* **1993**, *58*, 1672-1679.
[4]   a) C. H. Martin, H. Dhamankar, H.-C. Tseng, M. J. Sheppard, C. R. Reisch, K. L. J. Prather, *Nat. Commun.* **2013**, *4*, 1414; b) B. Hu, M. Prashad, D. Har, K. Prasad, O. Repič, T. J. Blacklock, *Org. Process Res. Dev.* **2007**, *11*, 90-93; c) H. S. Lee, D. H. Kim, *Biorg. Med. Chem.* **2003**, *11*, 4685-4691; d) D. Zhang, M. A. Hillmyer, W. B. Tolman, *Macromolecules* **2004**, *37*, 8198-8200.
[5]   a) M. A. Keane, *Langmuir* **1997**, *13*, 41-50; b) C. J. Baddeley, *Top. Catal.* **2003**, *25*, 17-28; c) C. J. Baddeley, T. E. Jones, A. G. Trant, K. E. Wilson, *Top. Catal.* **2011**, *54*, 1348-1356.
[6]   a) P. Tsaousis, J. Ontaneda, L. Bignardi, R. A. Bennett, R. Grau-Crespo, G. Held, *J. Phys. Chem. C* **2018**, *122*, 6186-6194; b) R. E. J. Nicklin, A. Shavorskiy, F. A. Akgul, Z. Liu, R. A. Bennett, M. Sacchi, G. Held, *J. Phys. Chem. C* **2018**, *122*, 7720-7730.
[7]   T. E. Jones, C. J. Baddeley, *J. Mol. Catal. A-Chem.* **2004**, *216*, 223-231.
[8]   a) J. Ontaneda, R. E. J. Nicklin, A. Cornish, A. Roldan, R. Grau-Crespo, G. Held, *J. Phys. Chem. C* **2016**, *120*, 27490-27499; b) D. J. Watson, S. Acharya, R. E. J. Nicklin, G. Held, *Surf. Sci.* **2014**, *629*, 108-113.
[9]   M. A. Keane, G. Webb, *Chem. Commun.* **1991**, 1619-1621.
[10] M. A. Lopez Martinez, PhD Thesis, https://etheses.bham.ac.uk/id/eprint/1491/2/Lopez_11_PhD.pdf
[11]   T. Osawa, Y. Amaya, T. Harada, O. Takayasu, *J. Mol. Catal. A: Chem.* **2004**, *211*, 93-96.
[12]   a) M. A. Keane, *Can J. Chem.* **1994**, *72*, 372-381; b) M. A. Keane, *Catal. Lett.* **1993**, *19*, 197-209.
[13]   a) S. G. Kwon, T. Hyeon, *Small* **2011**, *7*, 2685-2702; b) S. Mourdikoudis, L. M. Liz-Marzán, *Chem. Mater.* **2013**, *25*, 1465-1476.
[14]   a) C. B. Murray, S. Sun, W. Gaschler, H. Doyle, T. A. Betley, C. R. Kagan, *IBM J. Res. Dev.* **2001**, *45*, 47-56; b) C. B. Murray, S. Sun, H. Doyle, T. Betley, *MRS Bull.* **2001**, *26*, 985-991.
[15]   a) S. Campisi, M. Schiavoni, E. C. Chan-Thaw, A. Villa, *Catalysts* **2016**, *6*; bJ. V. I. Timonen, E. T. Seppälä, O. Ikkala, R. H. A. Ras, *Angew. Chem. Int. Ed. Engl.* **2011**, *50*, 2080-2084; c) E. V. Shevchenko, D. V. Talapin, H. Schnablegger, A. Kornowski, Ö. Festin, P. Svedlindh, M. Haase, H. Weller, *JACS* **2003**, *125*, 9090-9101.
[16]   A. C. Johnston-Peck, J. Wang, J. B. Tracy, *ACS Nano* **2009**, *3*, 1077-1084.
[17]   a) K. Guo, H. Li, Z. Yu, *ACS Appl. Mater. Interfaces* **2018**, *10*, 517-525; b) J. Park, E. Kang, S. U. Son, H. M. Park, M. K. Lee, J. Kim, K. W. Kim, H. J. Noh, J. H. Park, C. J. Bae, J. G. Park, T. Hyeon, *Adv. Mater.* **2005**, *17*, 429-434.
[18]   F. Davar, Z. Fereshteh, M. Salavati-Niasari, *J. Alloys Compd.* **2009**, *476*, 797-801.
[19]   Y. Pan, R. Jia, J. Zhao, J. Liang, Y. Liu, C. Liu, *Appl. Surf. Sci.* **2014**, *316*, 276-285.
[20]   a) S. Carenco, C. Boissière, L. Nicole, C. Sanchez, P. Le Floch, N. Mézailles, *Chem. Mater.* **2010**, *22*, 1340-1349; b) M. Li, Y. Chen, N. Ji, D. Zeng, D.-L. Peng, *Mater. Chem. Phys.* **2014**, *147*, 604-610.
[21]   K. Mandel, F. Dillon, A. A. Koos, Z. Aslam, K. Jurkschat, F. Cullen, A. Crossley, H. Bishop, K. Moh, C. Cavelius, E. Arzt, N. Grobert, *Chem. Commun.* **2011**, *47*, 4108-4110.
[22]   B. D. Anderson, J. B. Tracy, *Nanoscale* **2014**, *6*, 12195-12216.
[23]   H. Loboué, C. Guillot-Deudon, A. F. Popa, A. Lafond, B. Rebours, C. Pichon, T. Cseri, G. Berhault, C. Geantet, *Catal. Today* **2008**, *130*, 63-68.
[24]   A. P. Grosvenor, M. C. Biesinger, R. S. C. Smart, N. S. McIntyre, *Surf. Sci.* **2006**, *600*, 1771-1779.
[25]   H. W. Nesbitt, D. Legrand, G. M. Bancroft, *Phys. Chem. Miner.* **2000**, *27*, 357-366.
[26]   a) P. E. R. Blanchard, A. P. Grosvenor, R. G. Cavell, A. Mar, *Chem. Mater.* **2008**, *20*, 7081-7088; bS. Carenco, D. Portehault, C. Boissière, N. Mézailles, C. Sanchez, *Chem. Rev.* **2013**, *113*, 7981-8065.
[27]   S. Tougaard, *QUASES-IMFP-TPP2M Software*, Version 2.2., Physics Department, Odense University, Denmark, 2000–2002.
[28]   a) R. Arrigo, M. E. Schuster, S. Abate, S. Wrabetz, K. Amakawa, D. Teschner, M. Freni, G. Centi, S. Perathoner, M. Hävecker, R. Schlögl, *ChemSusChem* **2014**, *7*, 179-194; b) R. Arrigo, M. E. Schuster, S. Abate, G. Giorgianni, G. Centi, S. Perathoner, S. Wrabetz, V. Pfeifer, M. Antonietti, R. Schlögl, *ACS Catal.* **2016**, *6*, 6959-6966.
[29]   G. Akgul, F. A. Akgul, Y. Ufuktepe, *Vacuum* **2014**, *99*, 211-215.
[30]   G. van der Laan, J. Zaanen, G. A. Sawatzky, R. Karnatak, J. M. Esteva, *Phys. Rev. B* **1986**, *33*, 4253-4263.
[31]   S. E. Habas, F. G. Baddour, D. A. Ruddy, C. P. Nash, J. Wang, M. Pan, J. E. Hensley, J. A. Schaidle, *Chem. Mater.* **2015**, *27*, 7580-7592.
[32]   H.-R. Seo, K.-S. Cho, Y.-K. Lee, *Mat. Sci. Eng. B* **2011**, *176*, 132-140.
[33]   Y. Chen, C. Li, J. Zhou, S. Zhang, D. Rao, S. He, M. Wei, D. G. Evans, X. Duan, *ACS Catal.* **2015**, *5*, 5756-5765.
[34]   a) Tarachand, V. Sharma, J. Singh, C. Nayak, D. Bhattacharyya, N. Kaurav, S. N. Jha, G. S. Okram, *J. Phys. Chem. C* **2016**, *120*, 28354-28362; b) J. Singh, N. Kaurav, N. P. Lalla, G. S. Okram, *J Mater. Chem. C* **2014**, *2*, 8918-8924.
[35]   J. Chen, Z. Duan, Z. Song, L. Zhu, Y. Zhou, Y. Xiang, D. Xia, *Appl. Surf. Sci.* **2017**, *425*, 448-460.
[36]   H. Winnischofer, T. C. R. Rocha, W. C. Nunes, L. M. Socolovsky, M. Knobel, D. Zanchet, *ACS Nano* **2008**, *2*, 1313-1319.
[37]   T. Ishizaki, K. Yatsugi, K. Akedo, *Nanomaterials* **2016**, *6*.

11

[38]   a) M. F. Sarac, R. M. Wilson, A. C. Johnston-Peck, J. Wang, R. Pearce, K. L. Klein, A. V. Melechko, J. B. Tracy, *ACS Appl. Mater. Interfaces* **2011**, *3*, 936-940; b) C. de Mello Donegá, P. Liljeroth, D. Vanmaekelbergh, *Small* **2005**, *1*, 1152-1162.
[39]   V. Humblot, S. Haq, C. Muryn, W. A. Hofer, R. Raval, *JACS* **2002**, *124*, 503-510.
[40]   A. Coelho, *J. Appl. Crystallogr.* **2018**, *51*, 210-218.
[41]   a) D. Balzar, in *Defect and Microstructure Analysis from Diffraction* (Eds.: R. L. Snyder, H. J. Bunge, J. Fiala), International Union of Crystallography, New York, **1999**; b) TOPAS Technical Reference, http://www.topas-academic.net/.
[42]   A. Dent, G. Cibin, S. Ramos, A. Smith, S. Scott, L. Varandas, M. Pearson, N. Krumpa, C. Jones, P. Robbins, *J. Phys. Conf. Ser.* **2009**, *190*, 012039.
[43]   B. Ravel, M. Newville, *J. Synchrotron Radiat.* **2005**, *12*, 537-541.

12

FULL PAPER

WILEY-VCH

Entry for the Table of Contents

FULL PAPER
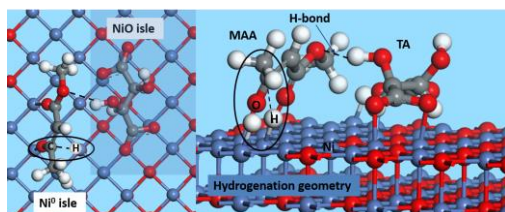
Ni nanoparticles with different electronic structure were synthetized via colloidal hot injection. In the asymmetric hydrogenation of methyl acetoacetate (MAA) to chiral methyl-3-hydroxy butyrate, (R)-selectivity is higher at low conversion and on oxidized surfaces of Ni nanoparticles, whereas no impact of particles size was observed. Our results indicate that during the hydrogenation reaction, the oxide phase enables a stronger chemisorption of the (*R, R*)-tartaric acid, which assists the favourable chemisorption of MAA on metallic Ni for the enantioselective hydrogenation to (*R*)-MHB.

Rosa Arrigo,* Simone Gallarati, Manfred E. Schuster, Jake Seymour, Diego Gianolio, Ivan da Silva, June Callison, Haosheng Feng, John E. Proctor, Pilar Ferrer, Federica Venturini, David Grinter and Georg Held

Page No. – Page No.

Influence of synthesis conditions on the structure of nickel nanoparticles and their reactivity in selective asymmetric hydrogenation